# The role of the North Atlantic Oscillation for projections of winter mean precipitation in Europe

Christine M. McKenna[1,1,1] and Amanda Maycock[1,1,1]

[1]University of Leeds

November 30, 2022

**Abstract**

Climate models generally project an increase in the winter North Atlantic Oscillation (NAO) index under a future high emissions scenario, alongside an increase in winter precipitation in northern Europe and a decrease in southern Europe. The extent to which future forced NAO trends are important for European winter precipitation trends and their uncertainty remains unclear. We show using the Multimodel Large Ensemble Archive that the NAO plays a small role in northern European mean winter precipitation projections for 2080-2099. Conversely, half of the model uncertainty in southern European mean winter precipitation projections is potentially reducible through improved understanding of the NAO. Extreme positive NAO winters increase in frequency in most models, coincident with mean NAO changes. These extremes also have more severe future precipitation impacts, largely because of background mean precipitation changes. This has implications for future resilience to extreme positive NAO winters, which already can have severe societal impacts.

# The role of the North Atlantic Oscillation for projections of winter mean precipitation in Europe

**C. M. McKenna[1] and A. C. Maycock[1]**

[1] School of Earth and Environment, University of Leeds, Leeds, UK

Corresponding author: Christine McKenna (C.McKenna1@leeds.ac.uk)

**Key Points:**

- The North Atlantic Oscillation (NAO) explains half of model spread in southern European winter precipitation change by 2080-2099 for RCP8.5
- Extreme positive NAO winters may increase in frequency in future by up to 35%, due to mean NAO change, but there is large model uncertainty
- Extreme positive NAO winters have more severe future precipitation impacts, with implications for resilience to this type of extreme season

## Abstract

Climate models generally project an increase in the winter North Atlantic Oscillation (NAO) index under a future high-emissions scenario, alongside an increase in winter precipitation in northern Europe and a decrease in southern Europe. The extent to which future forced NAO trends are important for European winter precipitation trends and their uncertainty remains unclear. We show using the Multimodel Large Ensemble Archive that the NAO plays a small role in northern European mean winter precipitation projections for 2080-2099. Conversely, half of the model uncertainty in southern European mean winter precipitation projections is potentially reducible through improved understanding of the NAO projections. Extreme positive NAO winters increase in frequency in most models as a consequence of mean NAO changes. These extremes also have more severe future precipitation impacts, largely because of mean precipitation changes. This has implications for future resilience to extreme positive NAO winters, which frequently have severe societal impacts.



## Plain Language Summary

Variations in atmospheric circulation over the North Atlantic are dominated by the North Atlantic Oscillation (NAO) pattern. A positive NAO phase is associated with a northward shift of the North Atlantic storm track, bringing wetter weather to northern Europe and drier weather to southern Europe. In future scenarios with increases in human-caused greenhouse gas emissions, climate models generally simulate an increase in the winter NAO, alongside an increase in winter precipitation in northern Europe and a decrease in southern Europe. However, it is unclear what role the NAO plays in future European winter precipitation trends. Here we show, using a large number of simulations from different climate models, that the NAO plays a small role in late 21$^{st}$ century northern European winter precipitation changes. Conversely, the NAO plays a sizable role in southern Europe. This is important because it suggests that uncertainty in southern European winter precipitation changes could be partly reduced with improved understanding of future NAO changes. Winters with an extremely positive NAO state are generally projected to increase in frequency and have larger precipitation impacts. This has implications for future resilience to these seasonal extremes, which already can have severe societal impacts including flooding and drought.

## 1 Introduction

The North Atlantic Oscillation (NAO) is the dominant mode of atmospheric circulation variability in the North Atlantic sector and exerts a strong influence on European winter weather and climate (Hurrell et al., 2003). A positive NAO phase is associated with a stronger North Atlantic eddy-driven jet stream and a northward displaced storm track. In winter, this brings mild and wet weather to northern Europe, and cold and dry weather to southern Europe.

The NAO is associated with the leading mode of interannual variability in European winter precipitation (Álvarez-García et al., 2019; Qian et al., 2000; Seager et al., 2020; Zveryaev, 2006) and can have significant societal impacts. For example, on interannual timescales the NAO influences precipitation and river flows in the Iberian Peninsula, with consequences for water availability for hydroelectricity production and intensive agriculture (Trigo et al., 2004). Prolonged winter periods with a predominantly positive NAO state are also connected to the occurrence of catastrophic flood events in northern Europe, with significant impacts on flood economic losses (Zanardo et al., 2019).

On longer timescales, climate models generally project an increase in the winter NAO index by the late 21$^{st}$ century under a high-emissions scenario (Christensen et al., 2013; Gillett & Fyfe, 2013; Lee et al., 2021; Stephenson et al., 2006), alongside an increase in winter precipitation in northern Europe and a decrease in southern Europe (Collins et al., 2013; Lee et al., 2021). While future atmospheric circulation change has been highlighted as a contributor to regional precipitation projections and their uncertainty (Deser et al., 2012, 2017; Fereday et al., 2018; Seager et al., 2010, 2014; Shepherd, 2014; Zappa et al., 2015), the extent to which future forced NAO trends are important for European mean winter precipitation trends and their uncertainty remains unclear. Furthermore, since extreme NAO winters are often associated with detrimental impacts, it is important to determine whether the projected NAO anomaly for the late 21$^{st}$ century under high-emissions alters the frequency of extreme positive NAO winters and their associated precipitation.

This study aims to determine the role of the NAO for projections of winter European precipitation. Specifically, we address:

1. What role do modeled forced trends in the NAO play in projections of European mean winter precipitation and their uncertainty?

2. Do models show an increase in the frequency of extreme positive NAO winters in the future and do mean NAO changes play a role?
3. Do extreme positive NAO winters have more severe precipitation impacts in the future and do mean NAO changes play a role?

## 2 Methods

### 2.1 Datasets

We use the Multimodel Large Ensemble Archive (MMLEA; Deser et al., 2020). The MMLEA contains large (16-100 member) initial-condition ensembles for seven Coupled Model Intercomparison Project Phase 5 (CMIP5) models (Table S1; Hazeleger et al., 2010; Jeffrey et al., 2013; Kay et al., 2015; Kirchmeier-Young et al., 2017; Maher et al., 2019; Rodgers et al., 2015; Schlunegger et al., 2019; Sun et al., 2018). While CMIP5 models may have stronger precipitation biases than higher resolution models (Roberts et al., 2019), the MMLEA dataset has various unique benefits. Initial-condition large ensembles provide a more accurate measure of the forced climate response and larger samples of relatively rare extreme winters. Multimodel large ensembles also allow us to examine structural model uncertainty in projections (Maher et al., 2021b). The MMLEA models are broadly representative of the spread in CMIP5 projections of the winter NAO index (McKenna & Maycock, 2021) and European winter precipitation (Figure S1), when accounting for internal variability.

We use historical and Representative Concentration Pathway (RCP) 8.5 simulations from the MMLEA models for the common period 1950-2099. RCP8.5 was chosen because only a small subset of the models is available for other RCPs. The analysis uses monthly-mean precipitation and mean sea level pressure (MSLP) data averaged over December to February (DJF).

The models are evaluated using observation-based MSLP data from the NOAA-CIRES-DOE 20$^{th}$ Century Reanalysis version 3 (20CRv3; Compo et al., 2011; Slivinski et al., 2019). This longer-term dataset was chosen to minimize the sampling errors associated with short observational records. Observed precipitation data is taken from E-OBS version 23.1e (Cornes et

al., 2018). We evaluate the models against the observations over a historical period common to all datasets (1951-2014; year is for January).

Data are regridded onto a 2° grid using bilinear interpolation for MSLP and a conservative remapping method in Climate Data Operators (Schulzweida, 2021) for precipitation.

### 2.2 Analysis and statistical methods

The long-term forced climate response is calculated as the ensemble-mean difference between the end-of-century (2080-2099) and near-present-day (1995-2014).

Following Stephenson et al. (2006) and Baker et al. (2018), the NAO index is defined as the difference in area-average MSLP between southern (90°W-60°E, 20°N-55°N) and northern (90°W-60°E, 55°N-90°N) boxes in the North Atlantic. The results are qualitatively similar for an empirical orthogonal function (EOF)-based NAO index.

The NAO-congruent part of a projected pattern of change in precipitation or MSLP is obtained by multiplying the projected change in NAO index by the historical NAO-precipitation or NAO-MSLP pattern. Using a future period to define the patterns gives similar results. Historical NAO-precipitation and NAO-MSLP patterns (Figure S2) are constructed from the regression slopes obtained by regressing historical (1951-2014) timeseries of DJF precipitation and MSLP in each grid-cell onto the NAO timeseries. All timeseries are linearly detrended. For MMLEA models, the patterns are defined for each member and then the ensemble-mean is calculated (Simpson et al., 2020). The modeled and observed NAO-precipitation patterns are highly correlated (Figure S2).

Precipitation changes are calculated as a percentage of the modeled 1995-2014 climatology. This reduces the influence of model climatological biases: for example, if a model simulates too little precipitation in a region climatologically, it will be unable to simulate a large decrease in precipitation in that region. Since this study concerns the NAO's role in Europe-wide precipitation projections, we calculate the area-average precipitation change over large areas of northern (45°N-72°N, 10°W-30°E) and southern (32°N-45°N, 10°W-30°E) Europe. These regions are defined based on broad areas of wetting to the north and drying to the south in the multimodel mean (MMM) precipitation projections for MMLEA.

95% confidence intervals on the MMLEA results are calculated as follows. For a model ensemble of size N, $10^4$ bootstrapped ensembles are created consisting of N members each by resampling with replacement whole ensemble members from the original N-member ensemble. Whole timeseries are sampled to preserve their temporal structure. The given quantity is calculated for each of the $10^4$ bootstrapped ensembles and confidence intervals are computed from the spread in the bootstrapped estimates of the quantity.

## 3 Results

### 3.1 Model evaluation

The MMLEA models are first evaluated against observations. Following Thompson et al. (2017), an MMLEA model is said to be indistinguishable from the observations if the observed value of a parameter lies within the 2.5%-97.5% range of inter-member spread in modeled values.

Figure S3 evaluates the modeled NAO-precipitation relationships for area-average precipitation in northern and southern Europe. In northern Europe, the observed and modeled relationships are indistinguishable based on the regression slope (Figure S3a) and correlation coefficient (Figure S3b). In southern Europe, however, the models generally simulate too little drying for a positive NAO index anomaly (Figure S3a) and generally underestimate the proportion of total precipitation variability that is NAO-congruent (Figure S3b).

Figure S4 evaluates the modeled NAO variability, using summary statistics for the distribution of historical annual winter NAO index anomalies. The standard deviation of the observed winter NAO distribution falls within the inter-member spread for every model except CSIRO-Mk3.6 and EC-EARTH, which have too low variability (Figure S4a). Therefore, CSIRO-Mk3.6 and EC-EARTH are not used for the results on extreme NAO winters (Section 3.3). All MMLEA models have a skewness and kurtosis that is indistinguishable from the observations (Figure S4b,c).

### 3.2 Role of the NAO in European mean winter precipitation projections

Figure 1a shows the forced change in northern and southern European winter precipitation between the future and present-day, for each MMLEA model and the MMM. This is decomposed into an NAO-congruent part and a residual. The models are ordered from left (CanESM2) to right (GFDL-CM3) with increasing NAO index change. Maps of precipitation and MSLP change are shown for the MMM in Figure 1b and for each model in Figure S5.

In northern Europe, there is a future increase in winter precipitation in all MMLEA models (Figure 1a). The increase is 15% of the present-day climatology on average and ranges from 10%-20% across the models. The NAO contribution to the mean change is generally small, but as expected depends on the magnitude of the NAO trend. For models with the strongest NAO trends (GFDL-ESM2M, GFDL-CM3), the NAO contributes up to one-third of the mean change in northern European winter precipitation, but is otherwise small. In all models, the residual precipitation change accounts for the majority of the total precipitation change.

In southern Europe, winter precipitation decreases in the future by an average of 12% (Figure 1a). However, there is large uncertainty across the models, from no change in CanESM2 to a decrease of 25% in GFDL-CM3. The NAO's role in these precipitation trends is proportionately larger than for northern Europe, contributing to two-fifths of the total precipitation change on average and up to half in the model with the largest NAO trend (GFDL-CM3). There is a residual drying trend in southern Europe in all models, but this only dominates over the NAO-congruent precipitation change in three models within error (EC-EARTH, MPI-ESM-LR, GFDL-ESM2M).

We now examine the NAO's role for model structural uncertainty in projections of forced European winter precipitation change. Similar to Fereday et al. (2018), we calculate the fraction of total intermodel variance in precipitation change that is NAO-congruent as $\sigma_{NAO}^2/\sigma_{TOT}^2$ (Figure 1c), where $\sigma_{TOT}^2 = \sigma_{NAO}^2 + \sigma_{RES}^2$, $\sigma_{NAO}^2$ is the intermodel variance in ensemble-mean NAO-congruent precipitation change, and $\sigma_{RES}^2$ is the intermodel variance in ensemble-mean residual precipitation change (Figure S6). Figure 1c shows the NAO contributes to one-fifth and half of the intermodel variance in northern and southern European precipitation changes, respectively. For smaller regions around the dominant centers of action for the NAO-precipitation relationship (Figure S2), the NAO contributes to a larger proportion of the model uncertainty (Figure 1c).

We hypothesize a sizable part of the residual wetting in northern Europe arises from the warming climate and associated increases in specific humidity (Held & Soden, 2006; Manabe & Wetherald, 1980; Seager et al., 2014; Trenberth et al., 2003). Indeed, normalizing precipitation change by global-mean surface air temperature (GSAT) change results in residual and total northern European precipitation changes that are similar in magnitude across the models (Figure S7). While non-NAO-congruent circulation change may play a role in some models (e.g., CanESM2; Figure S5), there is no clear relationship between the residual circulation and northern European precipitation anomalies on average (Figure 1b). In southern Europe, GSAT change largely does not control the amount of drying (Figure S7; Zappa et al., 2015). On average the residual drying could be associated with non-NAO-congruent anticyclonic circulation anomalies (Figure 1b). Seager et al. (2014) show, however, that near-term future CMIP5-mean Mediterranean precipitation change is both thermodynamic and dynamic in origin.

### 3.3 Frequency and precipitation impacts of future extreme positive NAO winters

Anomalous precipitation during extreme positive NAO winters contributes to flooding in northern Europe and meteorological drought in the Iberian Peninsula (Trigo et al., 2004; Zanardo et al., 2019). Figure 2 shows future changes in the frequency of extreme positive NAO winters, defined where the NAO index exceeds the present-day 95$^{th}$ percentile. The model with a negative mean NAO index change (CanESM2) simulates a decrease in frequency of extreme positive NAO winters, while models with positive NAO index changes show increases in frequency of up to 35% (GFDL-CM3). The changes in frequency can be largely explained by the mean NAO index change (Figure 2; Figure S8a). While an increase in NAO variability likely contributes to part of the frequency changes in CESM1-CAM5, changes in NAO variability are not consistent across the MMLEA models (Figure S8b). Changes in the skewness and kurtosis of the annual NAO index distribution are not robust in any model (Figure S8c-d).

Figure 3 shows future versus present-day precipitation anomalies (relative to the present-day climatology) for northern and southern Europe during extreme positive NAO winters, defined where the NAO index exceeds the 95$^{th}$ percentile for the given period. For the present-day, extreme positive NAO winters are generally associated with 10% higher winter precipitation in northern Europe and 20% lower precipitation in southern Europe (Figure 3). In the future, all MMLEA models project an increase in wet anomaly in northern Europe during

extreme positive NAO winters, from two (MPI-ESM-LR, GFDL-ESM2M) to three times as large (CanESM2, CESM1-CAM5, GFDL-CM3). In southern Europe, models with a smaller mean NAO index change project little change in precipitation (CanESM2, CESM1-CAM5), while models with a larger NAO index change (GFDL-ESM2M, GFDL-CM3) project dry anomalies during strongly positive NAO winters that are around twice as large.

A simple explanation for why extreme positive NAO winters have more severe future precipitation impacts is that the shift in climatological mean precipitation causes a shift in precipitation associated with NAO extremes. Future changes in the NAO-precipitation relationship and/or NAO variability could also play a role (e.g., Deser et al., 2017; Osborn, 2011).

Figure 4 shows the future minus present-day difference in precipitation during extreme positive NAO winters, decomposed into climatological mean parts and an "other" part. The climatological mean changes include the part due to mean NAO index changes and a residual part (i.e., the NAO-congruent part and residual from Figure 1, respectively). This shows precipitation changes during extreme positive NAO winters are largely consistent with climatological mean changes. In northern Europe, the increase in precipitation is dominated by the mean residual changes, a sizable part of which may be associated with background thermodynamic effects in a warmer climate (Section 3.2; Seager et al., 2014). Mean NAO changes play a larger role in southern Europe than for northern Europe, contributing to around half of the total precipitation anomaly in models with larger NAO index changes (GFDL-ESM2M, GFDL-CM3).

In CESM1-CAM5 and GFDL-CM3, there is a non-climatological increase and decrease, respectively, in northern European precipitation anomaly during future extreme positive NAO winters, which is different from zero within error. A sizable part of this is explained by an increase and decrease in the NAO-precipitation relationship ($p<0.05$; not shown), with small contributions from an increase and decrease in interannual NAO variability (Figure S8b). However, projected changes in interannual NAO variability (Figure S8b) and in NAO-precipitation relationship strength (not shown) are not consistent across the MMLEA models.

## 4 Discussion and Conclusions

This study has examined the role of forced NAO changes for projections of winter mean European precipitation using multimodel initial-condition large ensembles from the MMLEA. We use this smaller multimodel ensemble because the CMIP archives typically do not provide enough ensemble members per model to isolate forced NAO changes from internal variability (McKenna & Maycock, 2021).

Despite the spread in late 21$^{st}$ century projections of the mean winter NAO index across MMLEA models under the RCP8.5 scenario (McKenna & Maycock, 2021), the pattern of mean winter precipitation change is similar across models with wetting in northern Europe and drying in southern Europe. In northern Europe, the NAO only contributes up to one-third of the precipitation change in a given model and explains one-fifth of the intermodel spread. The NAO plays a larger role in southern Europe, contributing up to half of the precipitation change and explaining half of the intermodel spread. The NAO is relatively more important for precipitation change in certain smaller regions, including northwest Europe and the Iberian Peninsula, than at a continental scale.

Stephenson et al. (2006) found the NAO plays little role in mean winter precipitation projections for both northern and southern Europe. A direct comparison with our results is difficult, however, because they: 1) used an early generation of climate models (CMIP2); 2) had only one ensemble member available per model; and 3) analyzed idealized $CO_2$-only forcing simulations. In southern Europe or the Mediterranean, Zappa et al. (2015) and Fereday et al. (2018) show that future atmospheric circulation change contributes >50% of the CMIP5-mean winter precipitation response and 75%-80% of the intermodel spread. Our results suggest a large part of the forced component of the spread could be reduced by better understanding the causes of model uncertainty in NAO projections. In northern Europe, Fereday et al. (2018) also find little role of future atmospheric circulation change for CMIP5-mean winter precipitation change, but there is larger intermodel spread from circulation than found here. This discrepancy partly reflects that we specifically consider NAO-congruent circulation changes and, also, intermodel spread in CMIP5 precipitation projections is inflated by internal variability in atmospheric circulation, which the MMLEA models reduce (Deser et al., 2017; Figure S1). The additional

spread in Fereday et al. (2018)'s northern European precipitation projections arises from their use of monthly rather than seasonal trends and different methodological choices (e.g., expressing precipitation changes relative to the E-OBS climatology).

Second, we examine future changes in the frequency of extreme positive ($\geq 95^{th}$ percentile) NAO winters, which are often associated with severe societal impacts. The MMLEA models generally project an increase in extreme positive NAO winter frequency, largely due to a positive shift in mean NAO index. The increase can be up to 35% – i.e., a 1-in-20 year winter becomes a 2-in-5 year winter – but large intermodel spread in the magnitude of mean NAO index changes results in large model uncertainty in extreme frequency changes.

Third, we show extreme positive NAO winters have more severe precipitation impacts in future in all MMLEA models. In particular, future extreme positive NAO winters have northern European wet anomalies that are two to three times larger than in the present-day and southern European dry anomalies that are up to two times larger. Mean NAO index changes contribute up to half of the southern European precipitation changes. Across the MMLEA models, however, the most robust Europe-wide contribution is from non-NAO-congruent changes in climatological winter precipitation. Specifically, the larger precipitation anomalies during future extreme positive NAO winters arise from NAO-induced precipitation anomalies similar to present-day, superposed onto a future background climatology that constructively interferes with the NAO-precipitation pattern. This result implies a future decrease in our resilience to this type of seasonal extreme, which can already have severe societal impacts. This is an important consideration for policymakers involved in climate adaptation.

Model biases could influence this study's results. For example, the MMLEA models may underestimate NAO-congruent changes in southern European precipitation given the too-weak NAO-precipitation relationship in this region. They may also underestimate future increases in northern European precipitation as compared to higher resolution models (Moreno-Chamarro et al., 2021). Multiple Regional Climate Model initial-condition large ensembles are now becoming available (Maher et al., 2021a), which could be used to further examine the influence of biases. Importantly, models have been shown to underestimate forced NAO variability by a factor of two on seasonal timescales (Baker et al., 2018; Dunstone et al., 2016; Eade et al., 2014; Scaife & Smith, 2018; Scaife et al., 2014) and ten on decadal timescales (Smith et al., 2020). If models

also underestimate multidecadal forced NAO variability, late 21st century NAO-congruent changes in European winter mean precipitation may be underestimated. Future work should examine whether modeled multidecadal NAO variability has a too-low signal-to-noise ratio. Understanding the mechanisms responsible for intermodel spread in future forced NAO changes could provide an important constraint on the spread in southern European mean winter precipitation projections.

## Acknowledgments

CMM and ACM were supported by the European Union's Horizon 2020 research and innovation programme under grant agreement No 820829 (CONSTRAIN project). ACM was supported by The Leverhulme Trust. We acknowledge the U.S. CLIVAR Working Group on Large Ensembles for providing the MMLEA data, the E-OBS dataset from the EU-FP6 project UERRA (https://www.uerra.eu) and the Copernicus Climate Change Service, and the data providers in the ECA&D project (https://www.ecad.eu). We acknowledge the World Climate Research Programme's Working Group on Coupled Modelling, which is responsible for CMIP, and thank the climate modeling groups (see Table S2) for producing and making available their model output. For CMIP the U.S. Department of Energy's Program for Climate Model Diagnosis and Intercomparison provides coordinating support and led development of software infrastructure in partnership with the Global Organization for Earth System Science Portals.

## Data Availability Statement

The Multimodel Large Ensemble Archive data can be accessed at http://www.cesm.ucar.edu/projects/community-projects/MMLEA/. The GFDL-ESM2M large ensemble data used here can be accessed from the Princeton Large Ensemble Archive through Globus (https://www.sarahschlunegger.com/large-ensemble-archive). 20CRv3 can be downloaded from https://psl.noaa.gov/data/gridded/data.20thC_ReanV3.html and E-OBS from https://surfobs.climate.copernicus.eu/dataaccess/access_eobs.php. The CMIP5 precipitation data were downloaded from CEDA/JASMIN (timestamp of 23 May 2022); these are publicly

334 available through the Earth System Grid Federation at https://esgf-
335 index1.ceda.ac.uk/projects/cmip5-ceda/.

336

337 **References**

338 Álvarez-García, F. J., OrtizBevia, M. J., Cabos, W., Tasambay-Salazar, M., & RuizdeElvira, A.
339 (2019). Linear and nonlinear links of winter European precipitation to Northern
340 Hemisphere circulation patterns. *Climate Dynamics, 52*, 6533–6555.
341 https://doi.org/10.1007/s00382-018-4531-6

342 Baker, L. H., Shaffrey, L. C., Sutton, R. T., Weisheimer, A., & Scaife, A. A. (2018). An
343 intercomparison of skill and overconfidence/underconfidence of the wintertime North
344 Atlantic Oscillation in multimodel seasonal forecasts. *Geophysical Research Letters, 45*,
345 7808–7817. https://doi.org/10.1029/2018GL078838

346 Christensen, J. H., Krishna Kumar, K., Aldrian, E., An, S. -I., Cavalcanti, I. F. A., de Castro, M.,
347 et al. (2013). Climate Phenomena and their Relevance for Future Regional Climate
348 Change. In T. F. Stocker, et al. (Eds.), *Climate Change 2013: The Physical Science Basis.*
349 *Contribution of Working Group I to the Fifth Assessment Report of the Intergovernmental*
350 *Panel on Climate Change* (pp. 1217–1308). Cambridge, UK, and New York, NY, USA:
351 Cambridge University Press. https://doi.org/10.1017/CBO9781107415324.028

352 Compo, G. P., Whitaker, J. S., Sardeshmukh, P. D., Matsui, N., Allan, R. J., Yin, X., et al.
353 (2011). The Twentieth Century Reanalysis Project. *Quarterly Journal of the Royal*
354 *Meteorological Society, 137*(654), 1–28. https://doi.org/10.1002/qj.776

355 Cornes, R., van der Schrier, G., van den Besselaar, E. J. M., & Jones. P. D. (2018). An Ensemble
356 Version of the E-OBS Temperature and Precipitation Datasets. *Journal of Geophysical*
357 *Research: Atmospheres, 123*(17), 9391–9409. https://doi.org/10.1029/2017JD028200

358 Deser, C., Hurrell, J. W., & Phillips, A. S. (2017). The role of the North Atlantic Oscillation in
359 European climate projections. *Climate Dynamics, 49*, 3141–3157.
360 https://doi.org/10.1007/s00382-016-3502-z

Deser, C., Lehner, F., Rodgers, K. B., Ault, T., Delworth, T. L., DiNezio, P. N., et al. (2020). Insights from Earth system model initial-condition large ensembles and future prospects. *Nature Climate Change, 10*, 277–286. https://doi.org/10.1038/s41558-020-0731-2

Deser, C., Phillips, A., Bourdette, V., & Teng, H. (2012). Uncertainty in climate change projections: the role of internal variability. *Climate Dynamics, 38*, 527–546. https://doi.org/10.1007/s00382-010-0977-x

Dunstone, N., Smith, D., Scaife, A., Hermanson, L., Eade, R., Robinson, N., et al. (2016). Skilful predictions of the winter North Atlantic Oscillation one year ahead. *Nature Geoscience, 9*, 809–814. https://doi.org/10.1038/ngeo2824

Eade, R., Smith, D., Scaife, A., Wallace, E., Dunstone, N., Hermanson, L., & Robinson, N. (2014). Do seasonal-to-decadal climate predictions underestimate the predictability of the real world? *Geophysical Research Letters, 41*(15), 5620–5628. https://doi.org/10.1002/2014GL061146

Fereday, D., Chadwick, R., Knight, J., & Scaife, A. A. (2018). Atmospheric Dynamics is the Largest Source of Uncertainty in Future Winter European Rainfall. *Journal of Climate, 31*(3), 963–977. https://doi.org/10.1175/JCLI-D-17-0048.1

Gillett, N. P., & Fyfe, J. C. (2013). Annular mode changes in the CMIP5 simulations. *Geophysical Research Letters, 40*(6), 1189–1193. https://doi.org/10.1002/grl.50249

Hazeleger, W., Severijns, C., Semmler, T., Ştefănescu, S., Yang, S., Wang, X., et al. (2010). EC-Earth. *Bulletin of the American Meteorological Society, 91*(10), 1357–1364. https://doi.org/10.1175/2010BAMS2877.1

Held, I. M., & Soden, B. J. (2006). Robust Responses of the Hydrological Cycle to Global Warming. *Journal of Climate, 19*(21), 5686–5699. https://doi.org/10.1175/JCLI3990.1

Hurrell, J. W., Kushnir, Y., Ottersen, G., & Visbeck, M. (2003). An overview of the North Atlantic Oscillation. In J. W. Hurrell, Y., et al. (Eds.), *The North Atlantic Oscillation: Climate Significance and Environmental Impact, Geophysical Monograph Series* (Vol.

134, pp. 1–35). Washington, DC: American Geophysical Union. https://doi.org/10.1029/134GM01

Jeffrey, S., Rotstayn, L., Collier, M., Dravitzki, S., Hamalainen, C., Moeseneder, C., et al. (2013). Australia's CMIP5 submission using the CSIRO-Mk3.6 model. *Australian Meteorological and Oceanographic Journal, 63*(1), 1–14. https://doi.org/10.22499/2.6301.001

Kay, J. E., Deser, C., Phillips, A., Mai, A., Hannay, C., Strand, G., et al. (2015). The Community Earth System Model (CESM) Large Ensemble project: A community resource for studying climate change in the presence of internal climate variability. *Bulletin of the American Meteorological Society, 96*(8), 1333–1349. https://doi.org/10.1175/BAMS-D-13-00255.1

Kirchmeier-Young, M. C., Zwiers, F. W., & Gillett, N. P. (2017). Attribution of extreme events in Arctic sea ice extent. *Journal of Climate, 30*(2), 553–571. https://doi.org/10.1175/JCLI-D-16-0412.1

Lee, J. -Y., Marotzke, J., Bala, G., Cao, L., Corti, S., Dunne, J. P., et al. (2021). Future Global Climate: Scenario-Based Projections and Near-Term Information. In Masson-Delmotte, V., et al. (Eds.), *Climate Change 2021: The Physical Science Basis. Contribution of Working Group I to the Sixth Assessment Report of the Intergovernmental Panel on Climate Change* (pp. 553–672). Cambridge, UK, and New York, NY, USA: Cambridge University Press. https://doi.org/10.1017/9781009157896.006

Maher, N., Milinski, S., & Ludwig, R. (2021a). Large ensemble climate model simulations: introduction, overview, and future prospects for utilising multiple types of large ensemble. *Earth System Dynamics, 12*, 401–418. https://doi.org/10.5194/esd-12-401-2021

Maher, N., Milinski, S., Suarez-Gutierrez, L., Botzet, M., Dobrynin, M., Kornblueh, L., et al. (2019). The Max Planck Institute Grand Ensemble: Enabling the exploration of climate system variability. *Journal of Advances in Modeling Earth Systems, 11*(7), 2050–2069. https://doi.org/10.1029/2019MS001639

Maher, N., Power, S. B., & Marotzke, J. (2021b). More accurate quantification of model-to-model agreement in externally forced climatic responses over the coming century. *Nature Communications, 12*, 788. https://doi.org/10.1038/s41467-020-20635-w

Manabe, S., & Wetherald, R. T. (1980). On the Distribution of Climate Change Resulting from an Increase in CO2 Content of the Atmosphere. *Journal of Atmospheric Sciences, 37*(1), 99–118. https://doi.org/10.1175/1520-0469(1980)037<0099:OTDOCC>2.0.CO;2

McKenna, C. M., & Maycock, A. C. (2021). Sources of uncertainty in Multimodel Large Ensemble projections of the winter North Atlantic Oscillation. *Geophysical Research Letters, 48*(14), e2021GL093258. https://doi.org/10.1029/2021GL093258

Moreno-Chamarro, E., Caron, L. P., Ortega, P., Tomas, S. L., & Roberts, M. J. (2021). Can we trust CMIP5/6 future projections of European winter precipitation? *Environmental Research Letters, 16*(5), 054063. https://doi.org/10.1088/1748-9326/abf28a

Osborn T. J. (2011). Variability and Changes in the North Atlantic Oscillation Index. In Vicente-Serrano S., Trigo R. (Eds.), *Hydrological, Socioeconomic and Ecological Impacts of the North Atlantic Oscillation in the Mediterranean Region. Advances in Global Change Research* (Vol. 46, pp. 9–22). Dordrecht, Netherlands: Springer. https://doi.org/10.1007/978-94-007-1372-7_2

Qian, B., Corte-Real, J., & Xu, H. (2000). Is the North Atlantic Oscillation the most important atmospheric pattern for precipitation in Europe? *Journal of Geophysical Research: Atmospheres, 105*(D9), 11901–11910. https://doi.org/10.1029/2000JD900102

Roberts, M. J., Baker, A., Blockley, E. W., Calvert, D., Coward, A., Hewitt, H. T., et al. (2019). Description of the resolution hierarchy of the global coupled HadGEM3-GC3.1 model as used in CMIP6 HighResMIP experiments. *Geoscientific Model Developments, 12*(12), 4999–5028. https://doi.org/10.5194/gmd-12-4999-2019

Rodgers, K. B., Lin, J., & Frölicher, T. L. (2015). Emergence of multiple ocean ecosystem drivers in a large ensemble suite with an Earth system model. *Biogeosciences, 12*(11), 3301–3320. https://doi.org/10.5194/bg-12-3301-2015

Scaife, A. A., Arribas, A., Blockley, E., Brookshaw, A., Clark, R. T., Dunstone, N., et al. (2014). Skillful long-range prediction of European and North American winters. *Geophysical Research Letters, 41*(7), 2514–2519. https://doi.org/10.1002/2014GL059637

Scaife, A. A., & Smith, D. (2018). A signal-to-noise paradox in climate science. *npj Climate and Atmospheric Science, 1*, 28. https://doi.org/10.1038/s41612-018-0038-4

Schlunegger, S., Rodgers, K. B., Sarmiento, J. L., Frölicher, T. L., Dunne, J. P., Ishii, M., & Slater, R. (2019). Emergence of anthropogenic signals in the ocean carbon cycle. *Nature Climate Change, 9*, 719–725. https://doi.org/10.1038/s41558-019-0553-2

Schulzweida, Uwe. (2021). CDO User Guide (Version 2.0.0). Zenodo. http://doi.org/10.5281/zenodo.5614769

Seager, R., Liu, H., Henderson, N., Simpson, I., Kelley, C., Shaw, T., et al. (2014). Causes of Increasing Aridification of the Mediterranean Region in Response to Rising Greenhouse Gases. *Journal of Climate, 27*(12), 4655–4676. https://doi.org/10.1175/JCLI-D-13-00446.1

Seager, R., Liu, H., Kushnir, Y., Osborn, T. J., Simpson, I. R., Kelley, C. R., & Nakamura, J. (2020). Mechanisms of Winter Precipitation Variability in the European–Mediterranean Region Associated with the North Atlantic Oscillation. *Journal of Climate, 33*(16), 7179–7196. https://doi.org/10.1175/JCLI-D-20-0011.1

Seager, R., Naik, N., & Vecchi, G. A. (2010). Thermodynamic and Dynamic Mechanisms for Large-Scale Changes in the Hydrological Cycle in Response to Global Warming. *Journal of Climate, 23*(17), 4651–4668. https://doi.org/10.1175/2010JCLI3655.1

Shepherd, T. (2014). Atmospheric circulation as a source of uncertainty in climate change projections. *Nature Geoscience, 7,* 703–708. https://doi.org/10.1038/ngeo2253

Slivinski, L. C., Compo, G. P., Whitaker, J. S., Sardeshmukh, P. D., Giese, B. S., McColl, C., et al. (2019). Towards a more reliable historical reanalysis: Improvements for version 3 of the Twentieth Century Reanalysis system. *Quarterly Journal of the Royal Meteorological Society, 145*(724), 2876–2908. https://doi.org/10.1002/qj.3598

Smith, D. M., Scaife, A. A., Eade, R., Athanasiadis, P., Bellucci, A., Bethke, I., et al. (2020). North Atlantic climate far more predictable than models imply. *Nature, 583*, 796–800. https://doi.org/10.1038/s41586-020-2525-0

Stephenson, D., Pavan, V., Collins, M., Junge, M., Quadrelli, R., & Participating CMIP2 Modelling Groups (2006). North Atlantic Oscillation response to transient greenhouse gas forcing and the impact on European winter climate: A CMIP2 multi-model assessment. *Climate Dynamics, 27*(4), 401–420. https://doi.org/10.1007/s00382-006-0140-x

Sun, L., Alexander, M., & Deser, C. (2018). Evolution of the global coupled climate response to Arctic Sea ice loss during 1990–2090 and its contribution to climate change. *Journal of Climate, 31*(19), 7823–7843. https://doi.org/10.1175/JCLI-D-18-0134.1

Thompson, V., Dunstone, N. J., Scaife, A. A., Smith, D. M., Slingo, J. M., Brown, S., & Belcher, S. E (2017). High risk of unprecedented UK rainfall in the current climate. *Nature Communications, 8*, 107. https://doi.org/10.1038/s41467-017-00275-3

Trenberth, K. E., Dai, A., Rasmussen, R. M., & Parsons, D. B. (2003). The Changing Character of Precipitation. *Bulletin of the American Meteorological Society, 84*(9), 1205–1218. https://doi.org/10.1175/BAMS-84-9-1205

Trigo, R. M., Pozo-Vázquez, D., Osborn, T. J., Castro-Díez, Y., Gámiz-Fortis, S., & Esteban-Parra, M. J. (2004). North Atlantic Oscillation influence on precipitation, river flow and water resources in the Iberian Peninsula. *International Journal of Climatology, 24*(8), 925–944. https://doi.org/10.1002/joc.1048

Zanardo, S., Nicotina, L., Hilberts, A. G. J., & Jewson, S. P. (2019). Modulation of economic losses from European floods by the North Atlantic Oscillation. *Geophysical Research Letters, 46*(5), 2563–2572. https://doi.org/10.1029/2019GL081956

Zappa, G., Hoskins, B. J., & Shepherd, T. G. (2015). The dependence of wintertime Mediterranean precipitation on the atmospheric circulation response to climate change.

*Environmental Research Letters, 10*(10), 104012. https://doi.org/10.1088/1748-9326/10/10/104012

Zveryaev, I. I. (2006). Seasonally varying modes in long-term variability of European precipitation during the 20th century. *Journal of Geophysical Research, 111,* D21116. https://doi.org/10.1029/2005JD006821

## Figure captions

**Figure 1:** Role of forced DJF NAO index change (ΔNAOI) in DJF precipitation projections (2080-2099 minus 1995-2014) for the MMLEA models. (a) Area-average precipitation anomalies in northern (blue) and southern (brown) Europe; regions are defined by blue and brown boxes in (b). Left bar: Total anomaly; Middle bar: NAO-congruent part; Right bar: Residual. Precipitation anomalies are shown as a percentage of the 1995-2014 climatology. Error bars show bootstrapped 95% confidence intervals. (b) Maps of multimodel mean (MMM) precipitation (shading) and MSLP (contours) anomalies; Figure S5 shows maps for each model. Contours range from −2 hPa (dashed) to 2 hPa (solid) in 1 hPa intervals. (c) Fraction of total intermodel variance in precipitation projections that is NAO-congruent; see Figure S6 for further explanation. Colored numbers indicate fractions for northern and southern European precipitation changes in (a).

**Figure 2:** Projected change (2080-2099 minus 1995-2014) in the frequency of extreme positive (≥95$^{th}$ percentile for 1995-2014) NAO winters for selected MMLEA models (see Section 3.1). Contribution of mean DJF NAO index change (ΔNAOI) is calculated by shifting the 1995-2014 distribution of annual DJF NAO index by ΔNAOI. Error bars show bootstrapped 95% confidence intervals.

**Figure 3:** Precipitation anomalies during extreme positive (≥95$^{th}$ percentile) NAO winters for 2080-2099 versus 1995-2014 in selected MMLEA models (see Section 3.1). (a) Area-average precipitation anomalies in northern (blue) and southern (brown) Europe; regions are defined by blue and brown boxes in (b). Left bar: 1995-2014 anomaly; Middle bar: 2080-2099 anomaly; Right bar: 2080-2099 anomaly minus 1995-2014 anomaly. Precipitation anomalies are shown as

a percentage of the 1995-2014 climatology and averaged over all extreme positive NAO winters. Error bars show bootstrapped 95% confidence intervals. ΔNAOI is the mean DJF NAO index change for 2080-2099 minus 1995-2014. The multimodel mean (MMM) is for the selected models only. (b) Maps of MMM precipitation (shading) and MSLP (contours) anomalies; Figure S9 shows maps for each model. Contours range from −10.5 hPa (dashed) to 6 hPa (solid) in 1.5 hPa intervals.

**Figure 4:** Decomposition of projected precipitation change (2080-2099 minus 1995-2014) during extreme positive (≥95$^{th}$ percentile) NAO winters in selected MMLEA models (see Section 3.1). (a) Area-average precipitation anomalies in northern (blue) and southern (brown) Europe; regions are defined by blue and brown boxes in (b). Far left bar: Total anomaly; Middle left bar: Part from mean DJF NAO index change (ΔNAOI, NAO part in Figure 1); Middle right bar: Part from mean residual change (residual in Figure 1); Far right bar: Non-climatological "other" part. Precipitation anomalies are shown as a percentage of the 1995-2014 climatology and averaged over all extreme positive NAO winters. Error bars show bootstrapped 95% confidence intervals. The multimodel mean (MMM) is for the selected models only. (b) Maps of MMM precipitation (shading) and MSLP (contours) anomalies. Contours range from −2 hPa (dashed) to 1 hPa (solid) in 1 hPa intervals.

**Figure 1.**

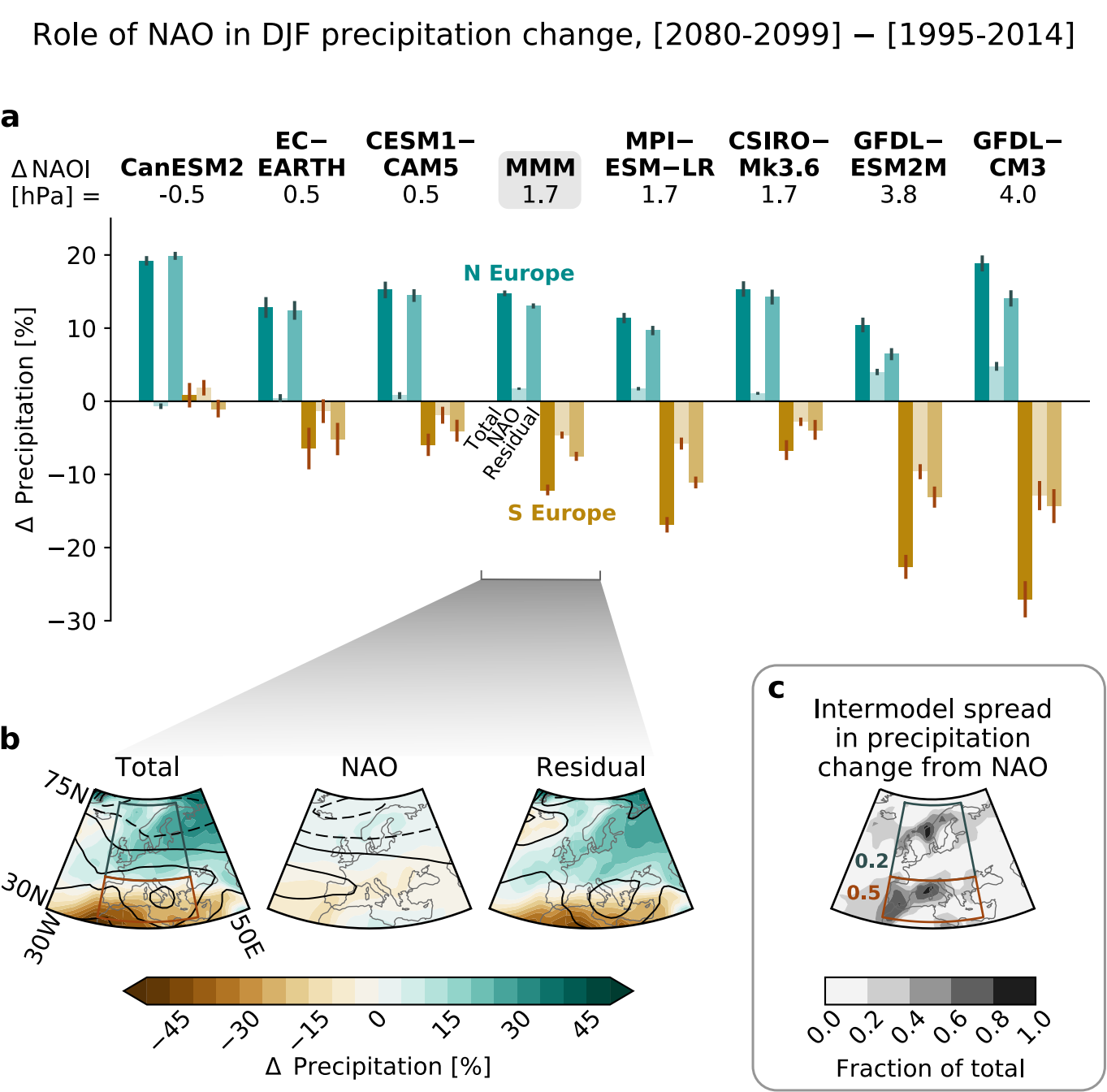
Role of NAO in DJF precipitation change, [2080-2099] − [1995-2014]
a
ΔNAOI [hPa] =
CanESM2 -0.5
EC−EARTH 0.5
CESM1−CAM5 0.5
MMM 1.7
MPI−ESM−LR 1.7
CSIRO−Mk3.6 1.7
GFDL−ESM2M 3.8
GFDL−CM3 4.0
Δ Precipitation [%]
N Europe
S Europe
Total
NAO
Residual
b
Total
NAO
Residual
75N
30N
30W
50E
−45 −30 −15 0 15 30 45
Δ Precipitation [%]
c
Intermodel spread in precipitation change from NAO
0.2
0.5
0.0 0.2 0.4 0.6 0.8 1.0
Fraction of total

**Figure 2.**

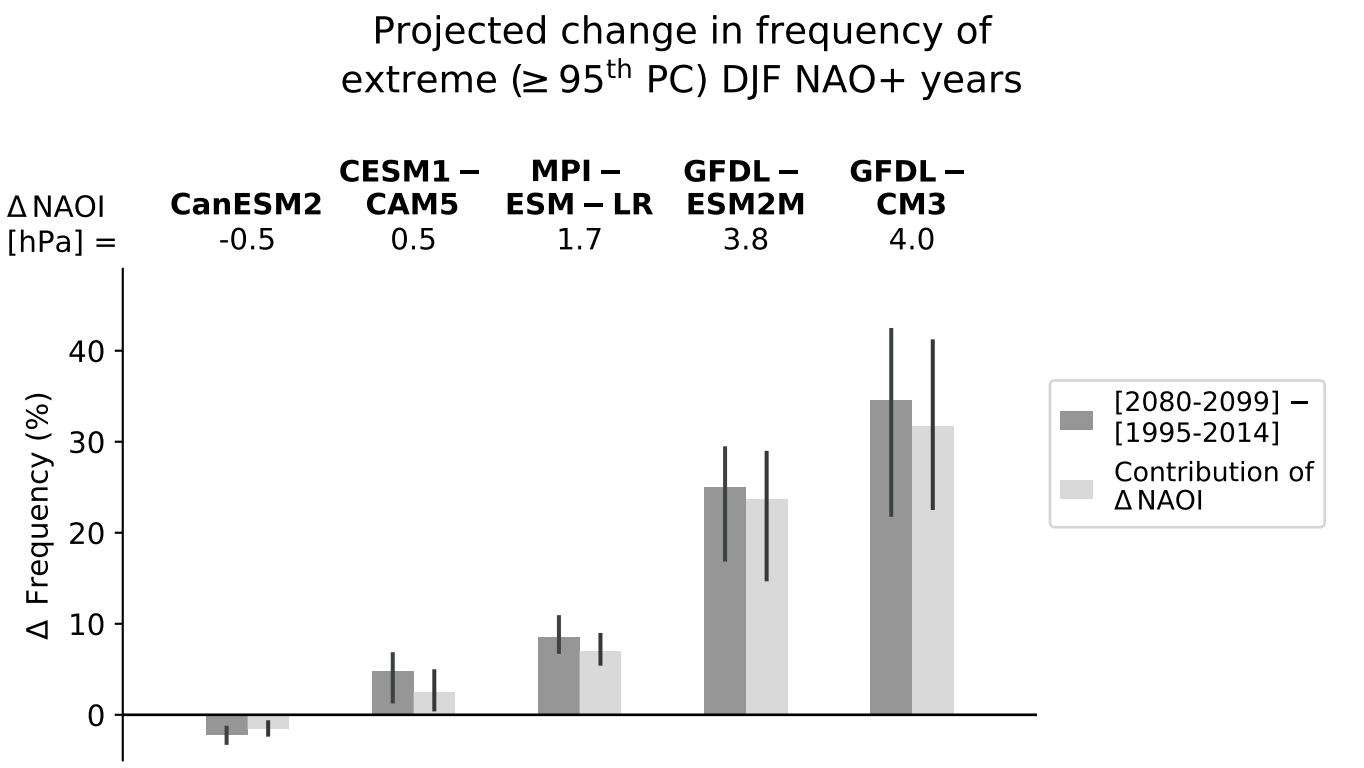
Projected change in frequency of
extreme (≥ 95th PC) DJF NAO+ years
ΔNAOI
[hPa] =
CanESM2
-0.5
CESM1 – CAM5
0.5
MPI – ESM – LR
1.7
GFDL – ESM2M
3.8
GFDL – CM3
4.0
Δ Frequency (%)
40
30
20
10
0
[2080-2099] – [1995-2014]
Contribution of ΔNAOI

**Figure 3.**

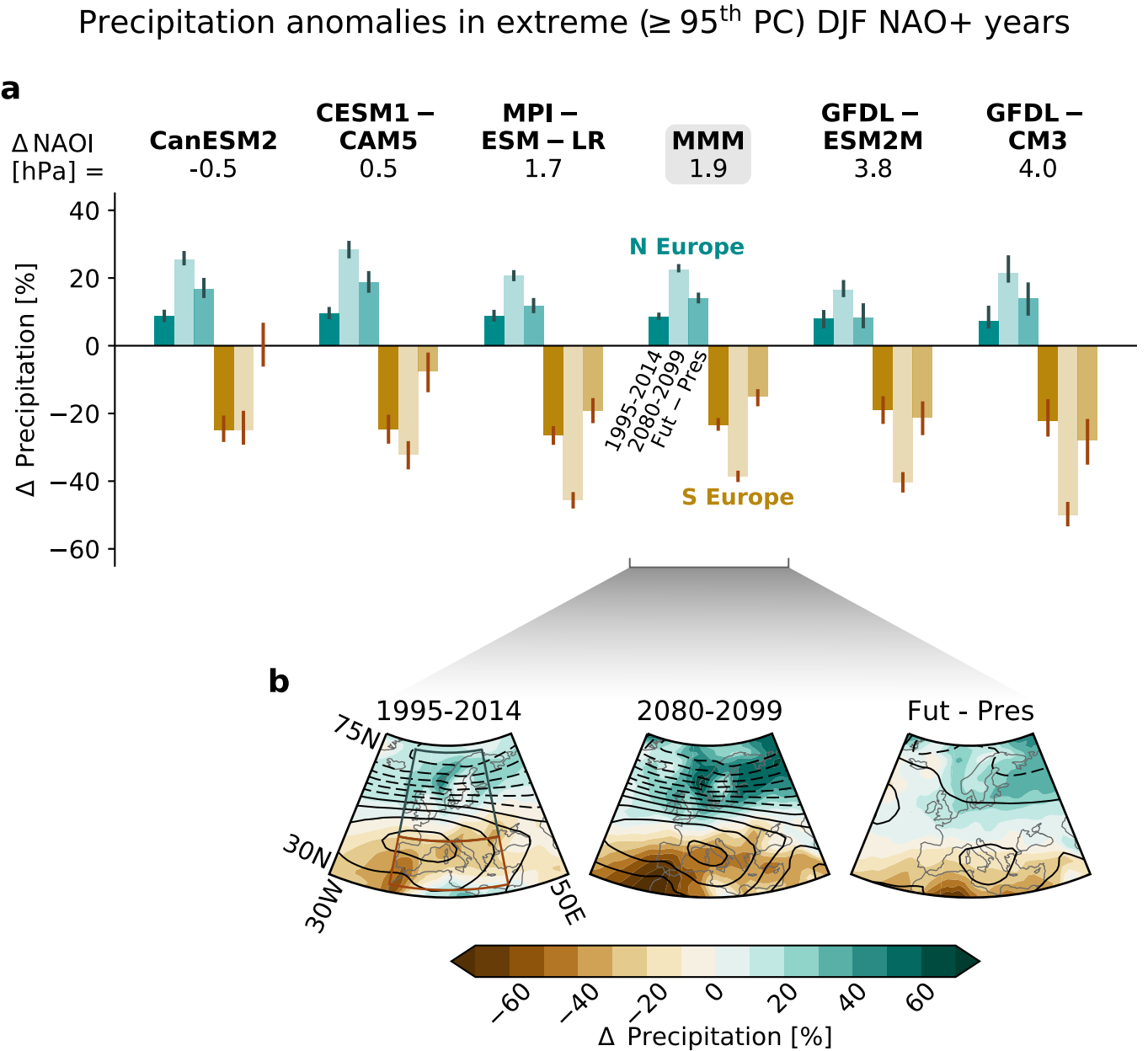
Precipitation anomalies in extreme (≥ 95th PC) DJF NAO+ years
a
ΔNAOI [hPa] =
CanESM2 -0.5
CESM1 – CAM5 0.5
MPI – ESM – LR 1.7
MMM 1.9
GFDL – ESM2M 3.8
GFDL – CM3 4.0
Δ Precipitation [%]
N Europe
S Europe
1995-2014
2080-2099
Fut – Pres
b
1995-2014
2080-2099
Fut - Pres
75N
30N
30W
50E
−60 −40 −20 0 20 40 60
Δ Precipitation [%]

**Figure 4.**

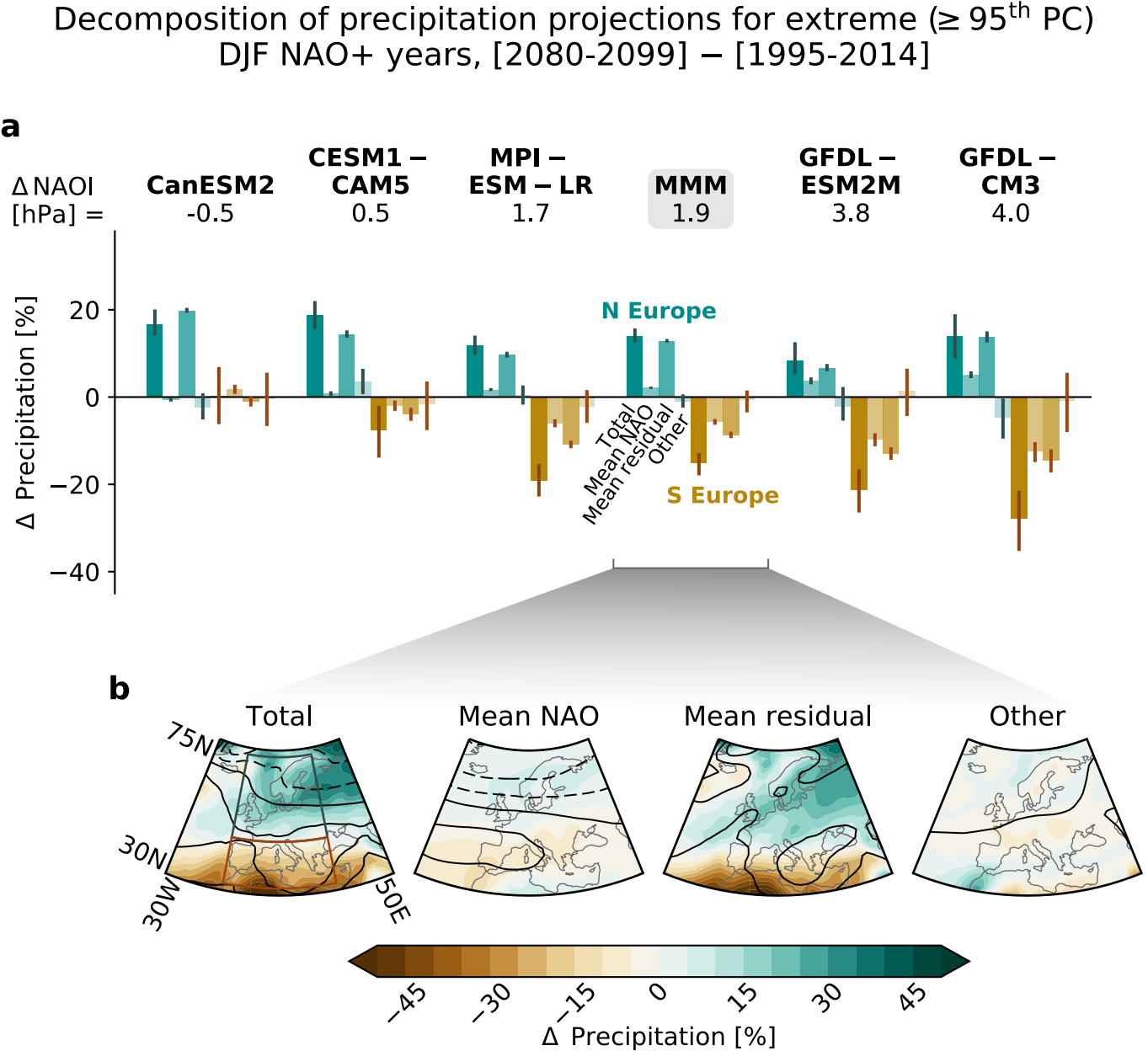
Decomposition of precipitation projections for extreme (≥ 95th PC)
DJF NAO+ years, [2080-2099] − [1995-2014]
a
ΔNAOI [hPa] =
CanESM2 -0.5
CESM1 − CAM5 0.5
MPI − ESM − LR 1.7
MMM 1.9
GFDL − ESM2M 3.8
GFDL − CM3 4.0
Δ Precipitation [%]
20
0
−20
−40
N Europe
S Europe
Total
Mean NAO
Mean residual
Other
b
Total
Mean NAO
Mean residual
Other
75N
30N
30W
50E
−45
−30
−15
0
15
30
45
Δ Precipitation [%]

*Geophysical Research Letters*

Supporting Information for

# The role of the North Atlantic Oscillation for projections of winter mean precipitation in Europe

C. M. McKenna[1] and A. C. Maycock [1]
[1] School of Earth and Environment, University of Leeds, Leeds, UK
Corresponding author: Christine McKenna (C.McKenna1@leeds.ac.uk)

## Contents of this file



## Introduction

This document contains tables and additional figures that provide further details on the datasets and methods used, the model evaluation process, and the results presented in the main text.

In particular, Table S1 provides details of the MMLEA model simulations used in the study. Table S2 provides details of the CMIP5 model simulations used in Figure S1. Figure S1 compares the intermodel spread in projections of future European mean winter precipitation change for the MMLEA models and the CMIP5 models. Figure S2 shows the historical winter NAO-MSLP and NAO-precipitation patterns for the MMLEA models and the observations; the modeled patterns are used in Figure 1 and Figure 4 to decompose MSLP and precipitation anomaly maps into an NAO-congruent part and a residual. Figure S3 evaluates the modeled NAO-precipitation relationships against the observations for area-average precipitation in northern and southern Europe. Figure S4 evaluates the modeled distributions of historical annual winter NAO index anomalies against the observed distribution. Figure S5 shows the maps from Figure 1b for all MMLEA models. Figure S6 explains the calculation of Figure 1c in further detail. Figure S7 shows a version of Figure 1 where the precipitation and MSLP changes are normalized by the change in global-mean surface air temperature. Figure S8 shows projected changes in the distributions of annual winter NAO index for selected MMLEA models. Figure S9 shows the maps from Figure 3b for all selected MMLEA models.

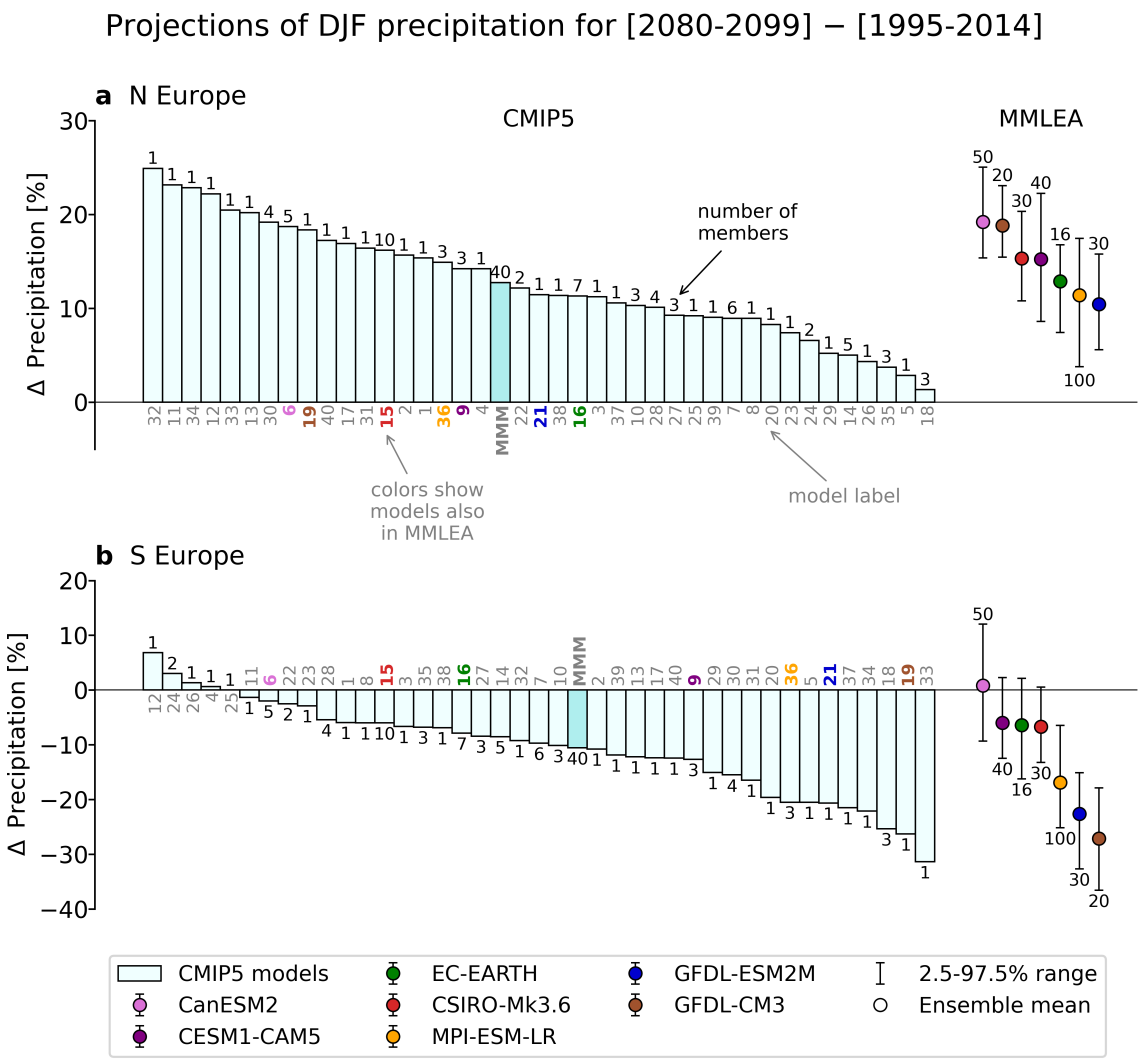


**Figure S1: Projected change (2080-2099 minus 1995-2014) in mean winter precipitation in (a) northern Europe and (b) southern Europe, for the CMIP5 and MMLEA models under the RCP8.5 scenario.** Precipitation anomalies are shown as a percentage of the 1995-2014 climatology. For CMIP5 models, ensemble means are shown if more than one ensemble member is available. Darker bar indicates the CMIP5 multimodel mean (MMM). Circles for MMLEA indicate the ensemble mean and whiskers indicate the 2.5%-97.5% range of responses across the ensemble members. A list of the CMIP5 model simulations used in this figure is given in Table S2.

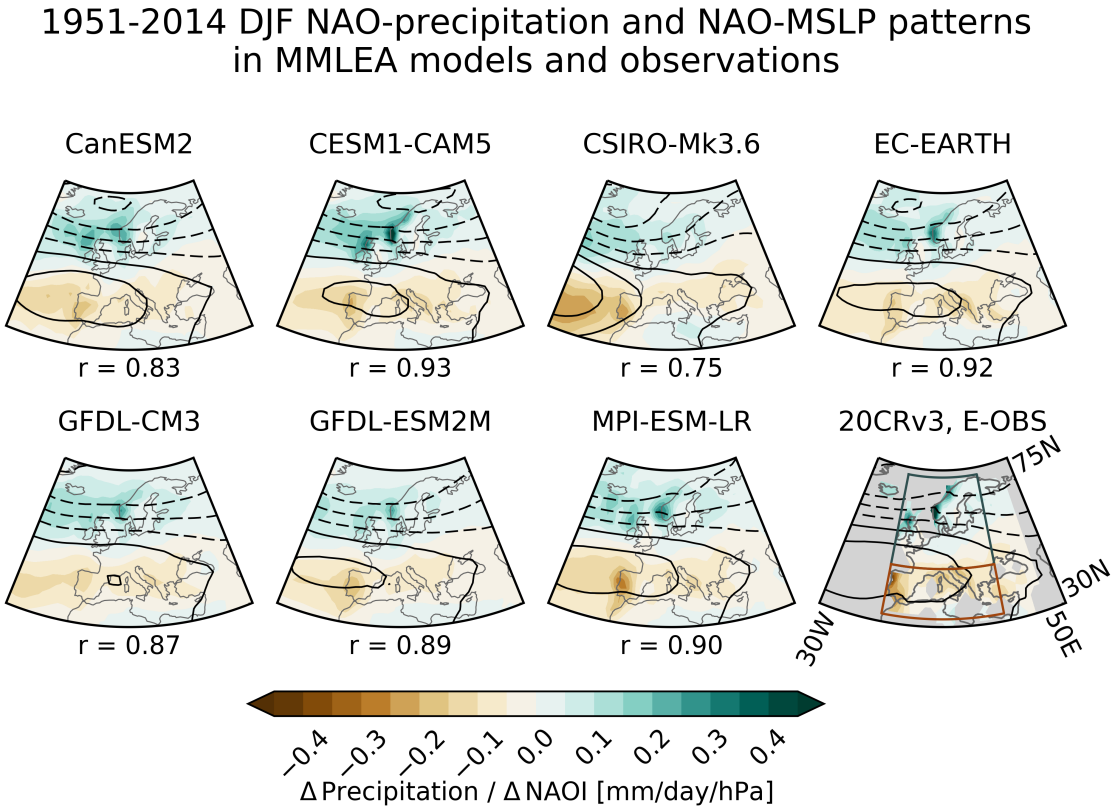


**Figure S2: Historical (1951-2014) DJF NAO-precipitation (shading) and NAO-MSLP (contours) patterns in the MMLEA models and observations.** Patterns are shown for a 1 hPa positive change in NAO index. MSLP contours range from −1.4 hPa (dashed) to 1 hPa (solid) in 0.4 hPa intervals. *r* is the area-weighted pattern correlation between the modeled and observed (20CRv3/E-OBS) NAO-precipitation patterns in regions where the observed pattern is not masked (non-gray shading). When calculating the observed NAO-precipitation pattern, masks are applied to any winter where more than one-third (30 days) of the E-OBS data is missing and any grid-cell where more than one-third (21 years) of winters are masked. Blue and brown boxes in the lower far-right panel define the northern and southern European regions used in the study, respectively.

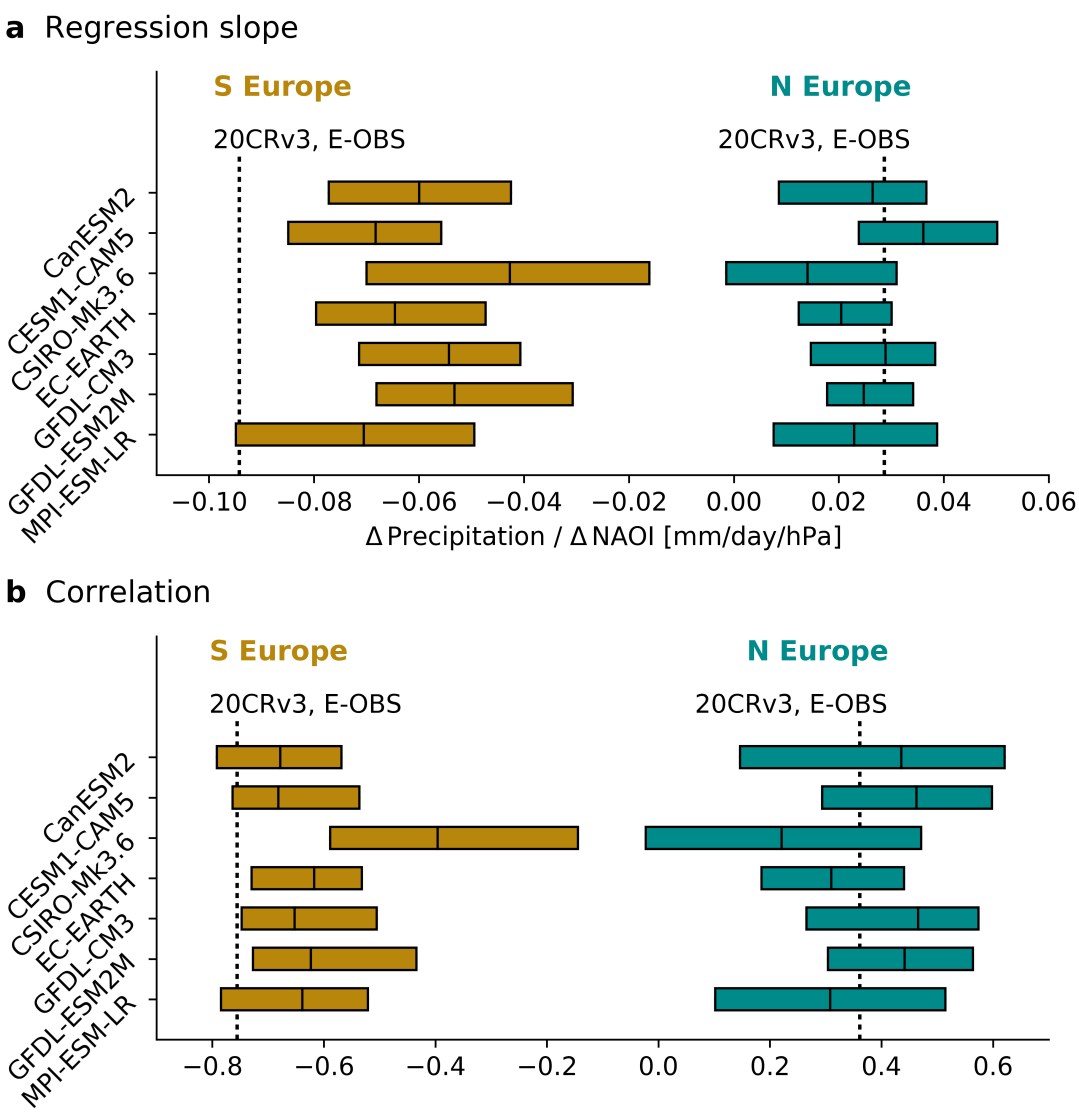


**Figure S3: Historical (1951-2014) DJF NAO-precipitation relationships for area-average precipitation in northern (blue) and southern (brown) Europe: an evaluation of the MMLEA models against the observations.** The relationships are evaluated in terms of (a) the regression slope (the parameter shown in Figure S2), and (b) the correlation coefficient. Colored boxes show the 2.5%-97.5% range and median value of each parameter across the ensemble members for each MMLEA model. Black vertical dashed lines show the values of each parameter for 20CRv3/E-OBS. Blue and brown boxes in the lower far-right panel of Figure S2 define the northern and southern European regions, respectively. Prior to calculating area-average northern and southern European precipitation for this figure, modeled data are masked in grid-cells where E-OBS data are masked (see Figure S2).

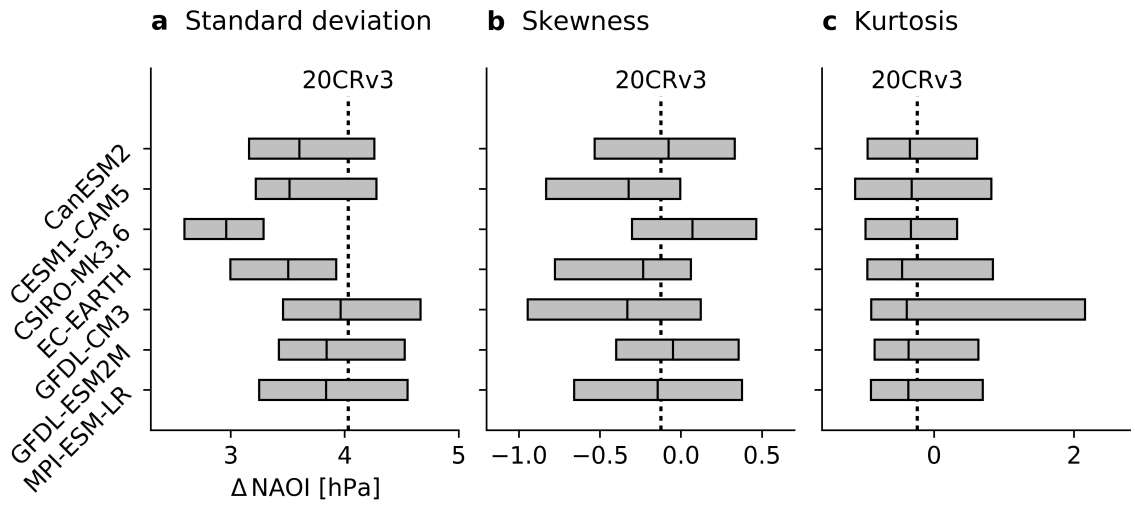


**Figure S4: Summary statistics for the distribution of historical (1951-2014) annual DJF NAO index anomaly: an evaluation of the MMLEA models against the observations.** The summary statistics evaluated are the (a) standard deviation, (b) skewness, and (c) kurtosis. Gray boxes show the 2.5%-97.5% range and median value of each statistic across the ensemble members for each MMLEA model. Black vertical dashed lines show the value of each statistic for 20CRv3. NAO index anomalies are defined relative to the 1995-2014 climatology.

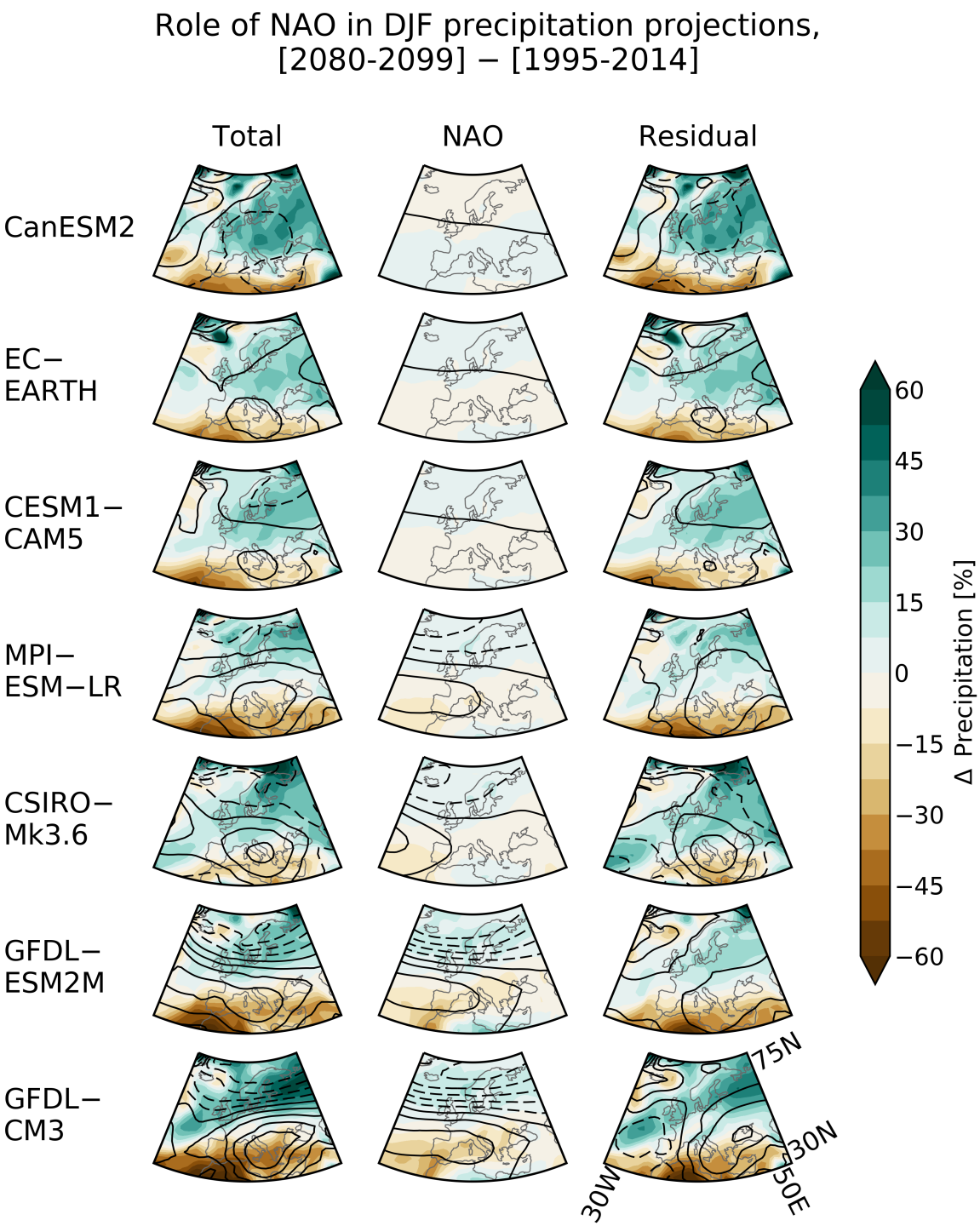


**Figure S5: Maps in Figure 1b for all MMLEA models.** Models are ordered from top to bottom with increasing forced DJF NAO index change. Contours range from −6 hPa (dashed) to 4 hPa (solid) in 1 hPa intervals.

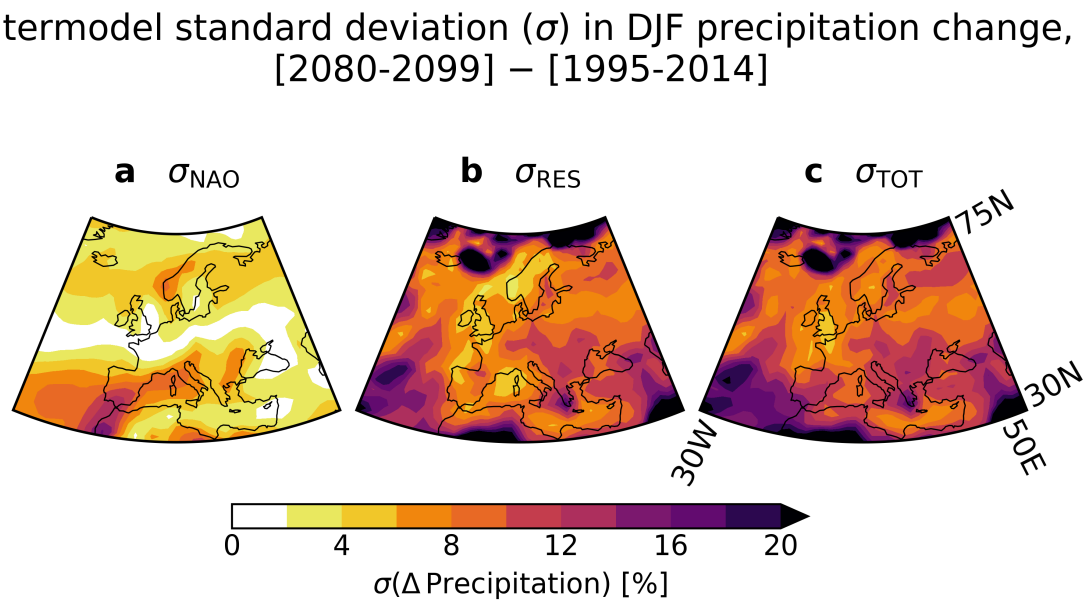


**Figure S6: Maps of the intermodel standard deviation, $\sigma$, in forced DJF precipitation projections (2080-2099 minus 1995-2014) for the MMLEA models. These maps are used to calculate Figure 1c.** (a) The intermodel standard deviation in NAO-congruent forced precipitation change, $\sigma_{NAO}$, calculated from the "NAO" column in Figure S5. (b) The intermodel standard deviation in residual forced precipitation change, $\sigma_{RES}$, calculated from the "Residual" column in Figure S5. (c) The sum of panels (a) and (b), $\sigma_{TOT}$, where $\sigma_{TOT}^2 = \sigma_{NAO}^2 + \sigma_{RES}^2$; note this is very similar to the intermodel standard deviation in total forced precipitation change, calculated from the "Total" column in Figure S5. Figure 1c shows the fraction of total intermodel variance in forced precipitation projections that is NAO-congruent, calculated as $\sigma_{NAO}^2/\sigma_{TOT}^2$ from panels (a) and (c).

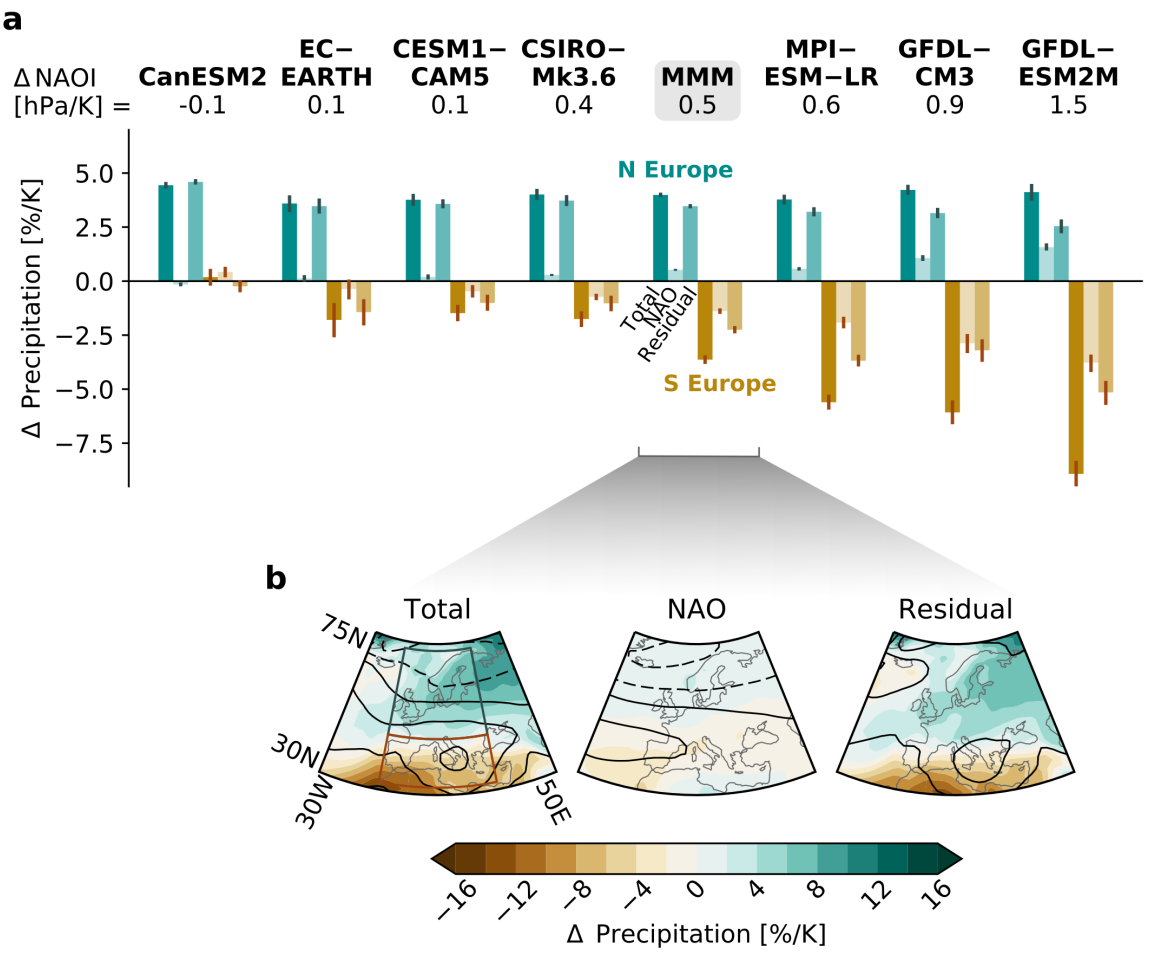


**Figure S7: Same as Figure 1a-b, but where the precipitation and MSLP changes are normalized by the change in global-mean surface air temperature (GSAT).** Models are ordered from left to right with increasing normalized forced DJF NAO index change (ΔNAOI); note this is a different order from Figure 1. GSAT changes from left to right are 4.3K (CanESM2), 3.6K (EC-EARTH), 4K (CESM1-CAM5), 3.8K (CSIRO-Mk3.6), 3.7K (MMM), 3K (MPI-ESM-LR), 4.5K (GFDL-CM3), and 2.5K (GFDL-ESM2M). Contours in (b) range from −0.6 hPa/K (dashed) to 0.6 hPa/K (solid) in 0.3 hPa/K intervals.

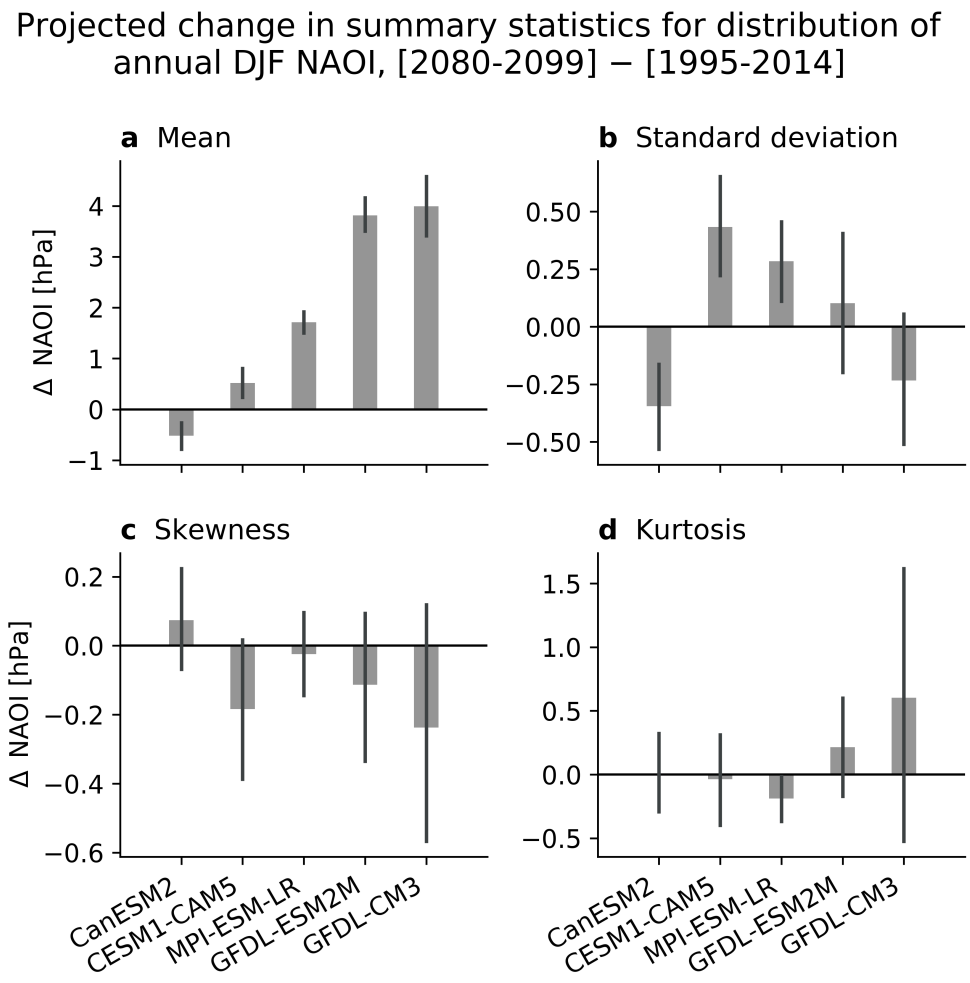


**Figure S8: Projected change (2080-2099 minus 1995-2014) in the summary statistics for the distribution of annual DJF NAO index, for selected MMLEA models (see Section 3.1).** The summary statistics evaluated are the (a) mean, (b) standard deviation, (c) skewness, and (d) kurtosis. Error bars show bootstrapped 95% confidence intervals.

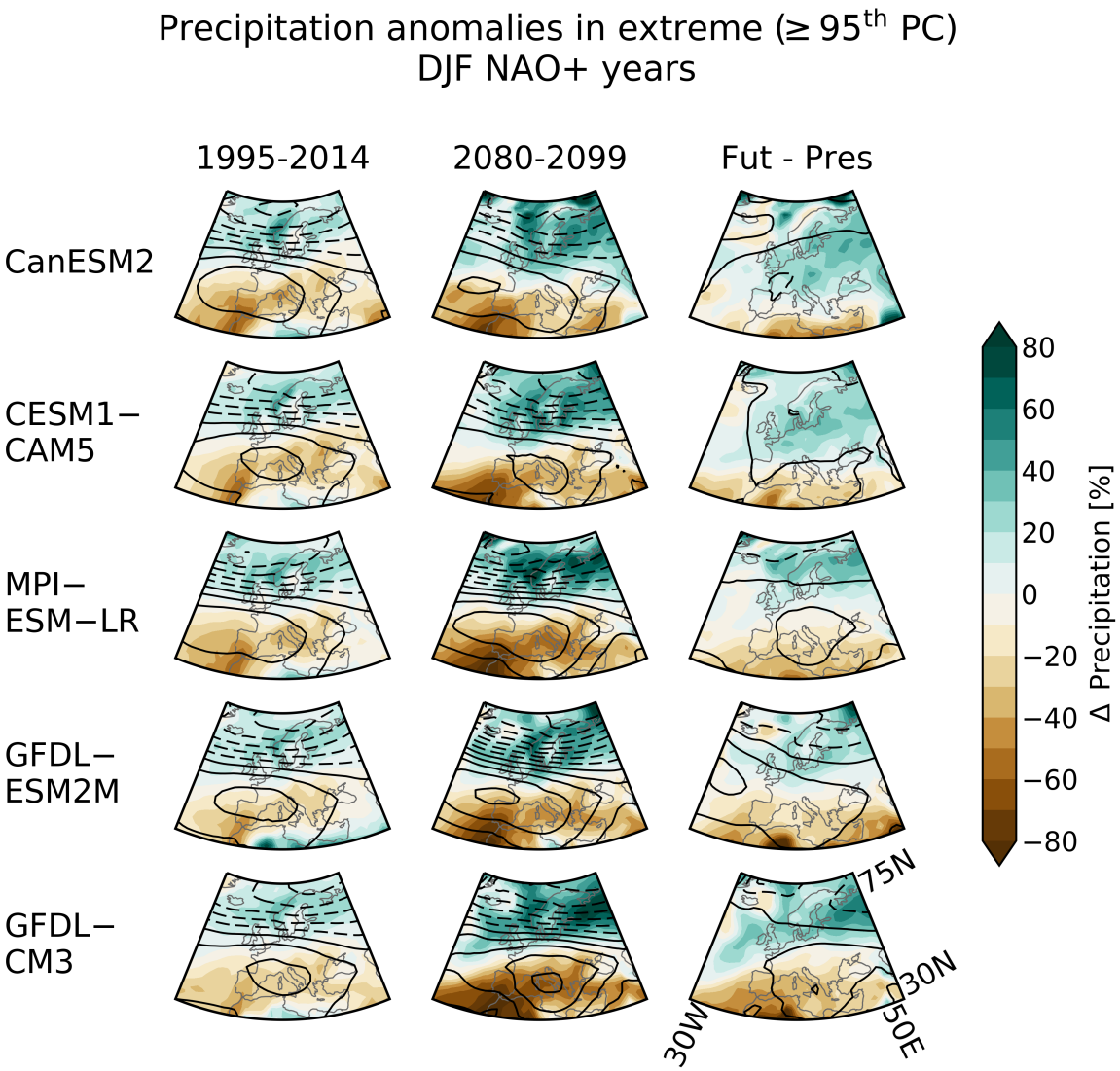


**Figure S9: Maps in Figure 3b for all selected MMLEA models (see Section 3.1).** Models are ordered from top to bottom with increasing mean DJF NAO index change. Contours range from −14 hPa (dashed) to 8 hPa (solid) in 2 hPa intervals.

**Table S1. Details of the MMLEA model simulations used in the study.** Simulations used are the historical and RCP8.5 runs. While the MMLEA does contain an ensemble for GFDL-ESM2M, for consistency with McKenna and Maycock (2021) we use a similar 30-member ensemble from the Princeton Large Ensemble Archive (Schlunegger et al., 2019).

| Model | Modeling Center | Years | Number of members | Reference |
|---|---|---|---|---|
| CanESM2 | CCCma | 1950–2100 | 50 | Kirchmeier-Young et al. (2017) |
| CESM1-CAM5 | NCAR | 1920–2100 | 40 | Kay et al. (2015) |
| CSIRO-Mk3.6 | CSIRO | 1850–2100 | 30 | Jeffrey et al. (2013) |
| EC-EARTH | EC-Earth Consortium | 1860–2100 | 16 | Hazeleger et al. (2010) |
| GFDL-CM3 | GFDL | 1920–2100 | 20 | Sun et al. (2018) |
| GFDL-ESM2M | GFDL | 1950–2100 | 30 | Rodgers et al. (2015); Schlunegger et al. (2019) |
| MPI-ESM-LR | MPI | 1850–2099 | 100 | Maher et al. (2019) |

**Table S2. Details of the CMIP5 model simulations used in Figure S1.** Simulations used are the historical and RCP8.5 runs. Numerical labels are for bars in Figure S1.

| Label | Model | Modeling Center | Number of members | Members used |
|---|---|---|---|---|
| 1 | ACCESS1.0 | CSIRO-BOM | 1 | r1i1p1 |
| 2 | ACCESS1.3 | | 1 | r1i1p1 |
| 3 | BCC-CSM1.1 | BCC | 1 | r1i1p1 |
| 4 | BCC-CSM1.1-M | | 1 | r1i1p1 |
| 5 | BNU-ESM | BNU | 1 | r1i1p1 |
| 6 | CanESM2 | CCCma | 5 | r1i1p1 – r5i1p1 |
| 7 | CCSM4 | NCAR | 6 | r1i1p1 – r6i1p1 |
| 8 | CESM1-BGC | NSF-DOE-NCAR | 1 | r1i1p1 |
| 9 | CESM1-CAM5 | | 3 | r1i1p1 – r3i1p1 |
| 10 | CESM1-WACCM | | 3 | r2i1p1 – r4i1p1 |
| 11 | CMCC-CESM | CMCC | 1 | r1i1p1 |
| 12 | CMCC-CM | | 1 | r1i1p1 |
| 13 | CMCC-CMS | | 1 | r1i1p1 |
| 14 | CNRM-CM5 | CNRM-CERFACS | 5 | r1i1p1, r2i1p1, r4i1p1, r6i1p1, r10i1p1 |
| 15 | CSIRO-Mk3.6.0 | CSIRO-QCCCE | 10 | r1i1p1 – r10i1p1 |
| 16 | EC-EARTH | ICHEC | 7 | r1i1p1, r2i1p1, r6i1p1, r8i1p1, r9i1p1, r12i1p1, r13i1p1 |
| 17 | FGOALS-g2 | LASG-CESS | 1 | r1i1p1 |
| 18 | FIO-ESM | FIO | 3 | r1i1p1 – r3i1p1 |

| Label | Model | Modeling Center | Number of members | Members used |
|---|---|---|---|---|
| 19 | GFDL-CM3 | NOAA-GFDL | 1 | r1i1p1 |
| 20 | GFDL-ESM2G | | 1 | r1i1p1 |
| 21 | GFDL-ESM2M | | 1 | r1i1p1 |
| 22 | GISS-E2-H | NASA-GISS | 2 | r1i1p1 – r2i1p1 |
| 23 | GISS-E2-H-CC | | 1 | r1i1p1 |
| 24 | GISS-E2-R | | 2 | r1i1p1 – r2i1p1 |
| 25 | GISS-E2-R-CC | | 1 | r1i1p1 |
| 26 | HadGEM2-AO | NIMR-KMA | 1 | r1i1p1 |
| 27 | HadGEM2-CC | MOHC | 3 | r1i1p1 – r3i1p1 |
| 28 | HadGEM2-ES | | 4 | r1i1p1 – r4i1p1 |
| 29 | INM-CM4 | INM | 1 | r1i1p1 |
| 30 | IPSL-CM5A-LR | IPSL | 4 | r1i1p1 – r4i1p1 |
| 31 | IPSL-CM5A-MR | | 1 | r1i1p1 |
| 32 | IPSL-CM5B-LR | | 1 | r1i1p1 |
| 33 | MIROC-ESM | MIROC | 1 | r1i1p1 |
| 34 | MIROC-ESM-CHEM | | 1 | r1i1p1 |
| 35 | MIROC5 | | 3 | r1i1p1 – r3i1p1 |
| 36 | MPI-ESM-LR | MPI-M | 3 | r1i1p1 – r3i1p1 |
| 37 | MPI-ESM-MR | | 1 | r1i1p1 |

| Label | Model | Modeling Center | Number of members | Members used |
|---|---|---|---|---|
| 38 | MRI-CGCM3 | MRI | 1 | r1i1p1 |
| 39 | NorESM1-M | NCC | 1 | r1i1p1 |
| 40 | NorESM1-ME | | 1 | r1i1p1 |